Preprints.org

Article

Nonlinear Dynamic Response of Nanocomposite Microbeams Array for Multiple Mass Sensing

Giovanni Formica [*] , Walter Lacarbonara , Hiroshi Yabuno

Article

Nonlinear Dynamic Response of Nanocomposite Microbeams Array for Multiple Mass Sensing

Giovanni Formica [1,*] **, Walter Lacarbonara** [2] **and Hiroshi Yabuno** [3]

[1] Department of Architecture, Roma Tre University, Italy; giovanni.formica@uniroma3.it
[2] Department of Structural and Geotechnical Engineering Sapienza University of Rome, Italy; walter.lacarbonara@uniroma1.it, marek.cetraro@uniroma1.it
[3] Faculty of Engineering, Information and Systems, University of Tsukuba, Japan; yabuno@esys.tsukuba.ac.jp
* Correspondence: giovanni.formica@uniroma3.it

Abstract: A nonlinear MEMS multimass sensor is investigated. The MEMS design consists of an array of nonlinear microcantilevers clamped to a shuttle mass which, in turn, is attached to a linear spring and a dashpot. The microcantilevers are made of a polymeric hosting matrix reinforced by aligned carbon nanotubes (CNT) with different CNT volume fractions in each cantilever so as to suitably tune the frequency bandwidth of the device. The advantages of a single input-single output (SISO) system are here exploited for the design, actuation and detection principles as in previous literature. The equations of motion of the MEMS micro mass sensor, whereby each of the microcantilevers attached to the shuttle mass is described by the nonlinear Euler-Bernoulli inextensible beam theory, are discretized via the Galerkin method. The frequency response curves of the device are obtained via a pathfollowing algorithm applied to the reduced-order model of the system. The linear as well as the nonlinear detection capabilities of the device are explored by computing the shifts of the frequency response peaks caused by the mass deposition onto one or more microcantilever tips. The mass sensor sensitivity estimated in the linear and nonlinear dynamic range shows that, for relatively large displacements, the accuracy of the added mass detectability can be improved due to the larger nonlinear frequency shifts at resonance.

Keywords: nanocomposite; microcantilever; mass sensing; frequency shifts; carbon nanotubes; nonlinear frequency response

---

1. Introduction

In the past decades MEMS have been subject to disruptinve developments in several fields of engineering both in research and applications (mainly, signal processing, actuation, and sensing). The lower power consumption and higher sensitivity are distinct advantages with respect to comparable macro devices. A general introduction about MEMS devices can be found in [1] with an overview of the fundamental concepts pertaining to linear and nonlinear dynamics of such systems. In recent years, a great deal of studies have sought to advance our understanding of the nonlinear dynamic behavior of nano/microresonators, which represent the main components of actual NEMS/MEMS devices [2–5]. Nonlinear dynamic aspects of electrostatically actuated microcantilevers are discussed in [6] while dynamics of the same systems subject to piezoelectric actuation are studied in [7].

Accurate models still need to achieve better agreement between analytical/numerical predictions and experiment results, and explore the use of new materials and technical capabilities. Initial imperfections of the structure, together with electrostatic actuation and nonlinear damping effects, are discussed in [8,9]. Moreover, systems with feedback loop control are investigated to enhance the sensitivity of the microdevices [10,11]. By restricting the attention to micromass sensing, the literature is becoming increasingly richer due to the present interest in gas detection, chemical agent detection, biological molecules and pollutant particles identification. In the mass/gas detection, different physical principles can be used to measure the different target substances. In [12–14] some electrical resistive detectors are investigated. In these studies the functioning of a semiconductor placed in an integrated

circuit aimed to measure target molecules such as SO_2 or NO_2 in order to perform environmental control or to measure the pollution associated with combustion chamber exhaust gases. Moreover, an example of a MEMS gas sensor using Knudsen force for hydrogen detection can be found in [15,16]. Therefore, MEMS gas sensors using the mechanical features of micro oscillators are of current interest. An overview on the working principles of these devices can be found in [17]. A micro mass sensor based on a microcantilever is discussed in [18]. This micromechanical resonator is used as gas sensor exploiting a working principle based on the detection of the beam natural frequency shift due to mass deposition onto the tip of the microbeam. In addition, similar works addressing microcantilevers used as sensor resonators to detect the chemical concentration of matter are found in [19,20]. On the other hand, a detection procedure is discussed in [21,22] where monitoring of the amplitudes of the localized vibration modes that vary when the system mass is perturbed was performed. A device made of two microcantilevers weakly coupled through an overhang working with localized modes is discussed in [23] while the use of these tools in highly viscous fluids is explored in [24,25]. Different kinds of electrostatic actuation are addressed in [26,27] to achieve large motions as well as higher sensitivity. In the field of NEMS, the performance of standalone carbon nanotube oscillators for mass detection is investigated in [28,29].

Numerous studies have been carried out to explore new mass detection strategies exploiting nonlinear effects. A parametrically excited clamped-clamped beam with cubic stiffness nonlinearity is explored as micromass sensor in [30]. The principle is based on the passage from the stable region to the unstable region across the transition curves of the Strutt diagrams. Also the jumps between the nonresonant and resonant branches occurring at the fold bifurcations along the frequency response curves are used as detection principle in [31,32]. Moreover, an electrostatically actuated microcantilever dynamic mass sensor was analytically investigated and experimentally tested in [33] to indirectly measure the added mass and its position along the span exploiting the frequency shift. The nonlinear dynamic behavior of an electrostatically actuated microbeam was studied in [34] to compare the different kinds of micromass detections according to the jumps at the bifurcation points, the frequency sweeps, and the frequency shifts of the resonant peaks. A specific study on the static and dynamic effects of the pull-in phenomena for a MEMS gas sensor can be found in [35].

In the present work, a single-input single-output (SISO) system is investigated making use of a path following algorithm optimized to tackle several degrees of freedom. The baseline idea of the SISO system can be found in [36] where a dynamic lumped system is studied numerically in the linear range. The working principle of the tool consists in the use of the shuttle mass motion both to excite the sensors and to read off the overall dynamic response of the system which includes the vibrations of all microcantilevers.

The analytical investigation via a perturbation technique of the design guidelines for SISO systems can be found in [37]. In the present work a different approach based on the eigenvalue analysis for a five-dof system is presented. One of the key aspects of the proposed design is the use of CNT nanocomposite material (*i.e.*, polymeric matrix hosting aligned CNTs forests) for the microcantilever detectors. An experimental and numerical study of the response of such nanostructured materials is given in [38–40]. Contrary to the conventional way of tuning the detector frequencies by changing their length, the proposed design consists of an array of equal-length beams having different CNT volume fractions which leads to easily tunable frequencies. The shuttle mass is a mass-spring-damper system while the microcantilevers clamped to the shuttle mass are modeled as nonlinear Euler-Bernoulli beams. The equations of motion are discretized via the Galerkin method and the system sensitivity is investigated for different cases such as the case of the system driven by a harmonic excitation or by an electrostatic actuation as well as the case of the system with one or more working sensor beams. The sensitivity of the device is computed in the linear and nonlinear dynamic ranges proving that the nonlinearities can enhance the detection capabilities.

2. Equations of motion for the nanocomposite microcantilevers

The SISO system investigated in the present study is depicted in Figure 1.
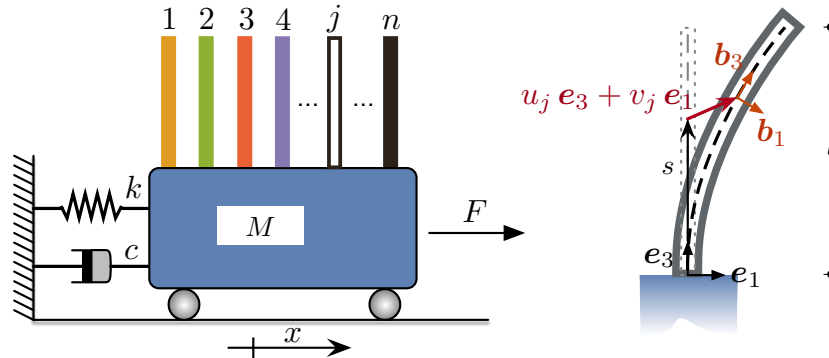

Figure 1. Array of nanocomposite microcantilevers clamped onto the shuttle mass. The microcantilevers are numbered from left to right. The coordinate x denotes the shuttle mass displacement, F the amplitude of harmonic direct excitation; on the right, a schematic representation of the deflection of the jth microcantilever together with the fixed and local frames and the coordinate s.

The flexural motion of the jth microcantilever is described by the nonlinear Euler-Bernoulli beam theory [41]. Let s and t be the arclength along the beam baseline and time, respectively, and let ∂_s and ∂_t denote differentiation with respect to s and t, respectively. The nonlinear equation of motion for the jth undamped microcantilever is given by the following integral-partial differential equation:

$$
\rho A(\partial_{tt} v_j \cos\theta_j - \partial_{tt} u_j \sin\theta_j) - \kappa_j N_j^* + \partial_{ss} M_j
$$
$$
+ \kappa_j \int_s^l \left[\rho A(\partial_{tt} u_j \cos\theta_j + \partial_{tt} v_j \sin\theta_j) - \kappa_j \partial_s M_j \right] d\xi = 0
\tag{1}
$$

where N_j^* is the normal force at the tip of the cantilever, which is due to the presence of the added mass at the tip denoted by m_j; ρA is the beam mass per unit length, with l being its span, while u_j and v_j are the axial and transverse (i.e., with respect to the fixed directions e_3 and e_1) displacements of the cantilevers, respectively. Furthermore, θ_j denotes the counterclockwise rotation of the beam cross section, κ_j is the flexural curvature, and $M_j = EJ_j^{\text{eq}}\kappa_j$ is the elastic bending moment, proportional to the equivalent flexural stiffness EJ_j^{eq} of the jth nanocomposite cantilever cross section. In particular, according to [39,42–44], such equivalent flexural stiffness is derived by a 3D continuum homogeneization model which provides the following expression:

$$
EJ_j^{\text{eq}} = \widehat{EJ}^{\text{eq}}(\phi_C, E_M, E_C, \nu_M, \nu_C)
\tag{2}
$$

where the equivalent stiffness depends on the volume fraction ϕ_C of the CNTs embedded in the polymeric hosting matrix, and of the isotropic elastic moduli of the two materials, Young's and Poisson's moduli E_C and ν_C, respectively for the CNTS, Young's and Poisson's moduli E_M and ν_M, respectively for the hosting polymeric matrix.

The boundary conditions for the jth microcantiliver considering the presence of the added mass m_j at its tip are:

$$
v_j(0,t) = x(t), \quad \partial_s v_j(0,t) = 0, \quad \partial_{ss} v_j(l,t) = 0,
$$
$$
EJ_j^{\text{eq}} \partial_{sss} v_j(l,t) = m_j \partial_{tt} v_j(l,t).
\tag{3}
$$

Note that the dynamic boundary condition involving the tip mass m_j is obtained via linearization of the fully nonlinear equation of motion for the lumped tip mass. Such equation enforces the balance of linear momentum at the cantilever tip expressed as

$$(N_j^* \mathbf{b}_3 + Q_j^* \mathbf{b}_1) = -m_j \left[\partial_{tt} u_j(l, t) \mathbf{e}_3 + \partial_{tt} v_j(l, t) \mathbf{e}_1 \right]. \tag{4}$$

where $(\mathbf{b}_1, \mathbf{b}_3)$ are the beam cross section-fixed unit vectors providing the current cross section orientation and the direction normal to it while $(\mathbf{e}_1, \mathbf{e}_3)$ indicate the fixed horizontal and vertical directions, respectively. Therefore, the jth tension N_j^* and shear force Q_j^* can be obtained as

$$N_j^* = -m_j \left[\cos \theta_j(l, t) \, \partial_{tt} u_j(l, t) + \sin \theta_j(l, t) \, \partial_{tt} v_j(l, t) \right], \tag{5}$$

$$Q_j^* = -m_j \left[- \sin \theta_j(l, t) \, \partial_{tt} u_j(l, t) + \cos \theta_j(l, t) \, \partial_{tt} v_j(l, t) \right]. \tag{6}$$

The subsequent linearization of equation (6) yields

$$Q_j^* = -m_j \partial_{tt} v_j(l, t). \tag{7}$$

By further expanding Equation (1) in Taylor series up to the third order adopting the moment-curvature law proposed in [42,43], and further developed in [44], expressing the longitudinal motion u_j as a function of the transverse motion v_j, the Euler-Bernoulli equations of motion governing the transverse dynamics of the jth microbeam with the tip mass m_j are cast in the form

$$\begin{aligned}
&\rho A \partial_{tt} v_j \left(1 - \tfrac{1}{2} (\partial_s v_j)^2 \right) + \rho A \partial_s v_j \int_0^s \left[\partial_s v_j \partial_{stt} v_j + (\partial_{st} v_j)^2 \right] d\xi \\
&+ \partial_{ss} v_j \int_s^l \rho A \left[\partial_s v_j \partial_{tt} v_j - \int_0^\xi \left(\partial_s v_j \partial_{stt} v_j + (\partial_{st} v_j)^2 \right) dz \right] d\xi \\
&+ \partial_{ss} M_j - \partial_{ss} v_j \int_s^l \partial_{ss} v_j \partial_s M_j \, d\xi \\
&+ m_j \partial_{ss} v_j \left[(\partial_s v_j)|_l (\partial_{tt} v_j)|_l + \int_0^l \left(\partial_s v_j \partial_{stt} v_j + (\partial_{st} v_j)^2 \right) d\xi \right] = 0
\end{aligned} \tag{8}$$

where v_j is the transverse deflection of the beam, the constitutive law for the bending moment is

$$M_j = E J_j^{\text{eq}} \kappa_j = E J_j^{\text{eq}} \left[\partial_{ss} v_j \left(1 + \tfrac{1}{2} (\partial_s v_j)^2 \right) \right] \quad \text{with} \quad \kappa_j = \partial_{ss} v_j \left(1 + \tfrac{1}{2} (\partial_s v_j)^2 \right)$$

Finally, the equation of motion for the shuttle mass is given by

$$M \partial_{tt} x + c \partial_t x + K x + \sum_{j=1}^{N_b} \partial_s M_j \big|_{s=0} = f \cos \Omega t \tag{9}$$

where x is the displacement of the shuttle mass M, c is the damping coefficient of the dashpot, k the spring constant, $f(t) = F \cos \Omega t$ with F and Ω being the excitation amplitude and frequency, respectively. The last term is the sum the shear forces of the N_b beams at the roots attached to the shuttle mass, on accounting for the relationship between shear force and moment gradient $Q = -\partial_s M$. In fact, the associated boundary conditions for the beams are the kinematic relations for the clamp and the mechanical boundary conditions at the tip

$$v_j(0, t) = \partial_s v_j(0, t) = x(t) = 0$$

and

$$M_j(l, t) = 0, \quad Q_j(l, t) = -m_j (\partial_{tt} x + \partial_{tt} v_j) \big|_{s=l}$$

Expressed in terms of displacements, the mechanical the boundary conditions at the tip become

$$EJ_j^{eq}\partial_{ss}v_j(l,t) = 0, \quad EJ_j^{eq}\partial_{sss}v_j(l,t) = m_j(\partial_{tt}x + \partial_{tt}v_j)\big|_{s=l}$$

We rescale the absolute displacements v_j of the jth beam and the shuttle mass displacement x by the length of the beams l, time by $1/\omega_c$ with $\omega_c^2 = EJ^{eq}/(\rho Al^4)$, where ρA is the mass per unit length of the reference beam whose bending stiffness is denoted by EJ^{eq}. By retaining the symbols s and t as the beam nondimensional arclength and time, respectively, and using the prime for space derivatives and the over dot for time derivatives, the ensuing nondimensional equations (8) become:

$$\mu\ddot{x}(t) + \xi\dot{x}(t) + K^* x(t) + \sum_{j=1}^{N_b}\alpha_j v_j'''(0,t) = f^* \cos\Omega^* t,$$

$$\begin{aligned}
&\mu_j\ddot{v}_j(s,t) + m_j^*\delta(s-1)\ddot{v}_j(s,t) + \xi_j\dot{v}_j(s,t) + \alpha_j v_j''''(s,t) \\
&+ \mu_j f_j^I[v(s,t),\dot{v}(s,t),\ddot{v}(s,t)] + \alpha_j f_j^R[v(s,t)] \\
&+ m_j^* f_j^{I*}[v(s,t),\dot{v}(s,t),\ddot{v}(s,t)] = 0, \quad \text{for } j = 1,\ldots,N_b
\end{aligned} \qquad (10)$$

where

$$\begin{aligned}
f_j^I[v,\dot{v},\ddot{v}] &= -\tfrac{1}{2}\ddot{v}_j(v_j')^2 + v_j''\int_{s^\star}^1\left[\ddot{v}_j v_j'\right]d\xi^\star + v_j'\int_0^{s^\star}\left[v_j'\ddot{v}_j\right]d\xi^\star \\
&\quad - v_j''\int_{s^\star}^1\left[\int_0^{s^\star}\left[v_j'\ddot{v}_j\right]d\xi^\star\right]ds^\star + v_j'\int_0^{s^\star}\left[(\dot{v}_j')^2\right]d\xi^\star \\
&\quad - v_j''\int_{s^\star}^1\left[\int_0^{s^\star}\left[(\dot{v}_j')^2\right]d\xi^\star\right]ds^\star,
\end{aligned}$$

$$f_j^R[v] = (v_j'')^3 + \tfrac{1}{2}v_j''''(v_j')^2 + 3v_j'''v_j''v_j' - v_j''\int_{s^\star}^1(v_j''v_j''' + \cdots)d\xi^\star,$$

$$f_j^{I*}[v,\dot{v},\ddot{v}] = v_j''\left[(v_j')\Big|_1(\ddot{v}_j)\Big|_1 - \int_0^1\left(v_j'\ddot{v}_j + (\dot{v}_j')^2\right)d\xi\right].$$

In the governing equations, we introduced the following nondimensional parameters:

$$\mu := M/(\rho Al), \quad \mu_j := \rho A_j/\rho A, \quad m_j^* := m_j/(\rho Al),$$

$$\xi := c/(\rho Al\omega_c), \quad \xi_j := c_j/(\rho A\omega_c),$$

$$K^* := K/(\rho Al\omega_c^2), \quad \alpha_j := EJ_j^{eq}/(\rho A\omega_c^2 l^4),$$

$$f^* := f/(\rho Al^2\omega_c^2), \quad \Omega^* := \Omega/\omega_c,$$

where m_j is the tip mass of the jth beam, ξ_j its damping coefficient, (μ, K^*, ξ) are the nondimensional mass, spring constant and damping coefficient of the shuttle mass, f^* and Ω^* are the nondimensional excitation amplitude and frequency, respectively.

We further introduce the beam deflections w_j relative to the shuttle mass according to $v_j(s,t) = w_j(s,t) + x(t)$. The equations of motion in terms of the relative beam deflections w_j take the following form:

$$\mu\ddot{x}(t) + \xi\dot{x}(t) + K^* x(t) + \sum_{j=1}^{N_b}\alpha_j w_j'''(0,t) = f^* \cos\Omega^* t,$$

$$\begin{aligned}
&\mu_j\left(\ddot{w}_j(s,t) + \ddot{x}(t)\right) + m_j^*\delta(s-1)\left(\ddot{w}_j(s,t) + \ddot{x}(t)\right) + \xi_j\dot{w}_j(s,t) + \alpha_j w_j''''(s,t) \\
&+ \alpha_j f_j^R[w(s,t)] + \mu_j f_j^I[w(s,t),\dot{w}(s,t),\ddot{w}(s,t)] + m_j^* f_j^{I*}[w(s,t),\dot{w}(s,t),\ddot{w}(s,t)] \\
&+ \mu_j g_j^I[w(s,t)]\ddot{x}(t) + m_j^* g_j^{I*}[w(s,t)]\ddot{x}(t) = 0, \quad \text{for } j = 1,\ldots,N_b,
\end{aligned} \qquad (11)$$

where

$$g_j^I[w] = -\tfrac{1}{2}(w_j')^2 + w_j'' \int_{s^\star}^1 \left[w_j' \right] d\xi^\star, \quad g_j^{I*}[w] = w_j''(w_j') \Big|_1 .$$

3. Modal analysis

The modal analysis of the SISO system here discussed is the first step towards the nonlinear analyses carried out on the Galerkin obtained reduced order models. Moreover, the variability of the eigenfrequencies of the SISO system reveals interesting preliminary results, thanks to the nanostructured nature of the materials constituting the microbeams.

Let the jth overall mode shape of the system be cast in the vector-valued form:

$$\mathbf{u}_j^\top = [X_j, \phi_{1,j}(s), \phi_{2,j}(s), \dots, \phi_{N_b,j}(s)] = [X_j, \phi_{k,j}(s)], \quad k = 1, \dots N_b \tag{12}$$

For further details see Appendix A. The substitution of the jth mode in the nondimensional kth beam equation and shuttle mass equation yields

$$-\mu_k \omega_j^2 \phi_{k,j} + \alpha_k \phi_{k,j}'''' = 0 \tag{13}$$

$$-\mu \omega_j^2 X_j + K^* X_j + \sum_k \alpha_k \phi_{k,j}'''(0) = 0 ; \tag{14}$$

the associated boundary conditions for the beams are

$$\phi_{k,j}(0) - X_j = 0 \quad \phi_{k,j}'(0) = 0 \tag{15}$$

$$\alpha_k \phi_{k,j}''(1) = 0, \quad \alpha_k \phi_{k,j}'''(1) + m_k^* \omega_j^2 \phi_{k,j}(1) = 0 \tag{16}$$

We multiply Equation (13) by $\phi_{k,i}$, integrate over $[0, 1]$ and sum the resulting projected equations for all beams; we multiply Equation (14) by X_i and sum the previously projected beam equations and the shuttle mass equation to obtain:

$$-\omega_j^2 \Bigg[\sum_{k=1}^{N_b} \mu_k \int_0^1 \phi_{k,i}\phi_{k,j}ds + \mu X_i X_j \Bigg] + \sum_{k=1}^{N_b} \alpha_k \int_0^1 \phi_{k,i}\phi_{k,j}''''ds \tag{17}$$

$$+ K^* X_i X_j + X_i \sum_{k=1}^{N_b} \alpha_k \phi_{k,j}'''(0) = 0$$

We further integrate by parts the bending terms in the beam equations to obtain

$$\int_0^1 \phi_{k,i}\phi_{k,j}''''ds = \phi_{k,i}\phi_{k,j}''' \big|_{s=0}^1 - \phi_{k,i}'\phi_{k,j}'' \big|_{s=0}^1 + \int_0^1 \phi_{k,i}''\phi_{k,j}''ds \tag{18}$$

Employing the boundary conditions (15) yields

$$\int_0^1 \phi_{k,i}\phi_{k,j}''''ds = -\phi_{k,i}(1)\omega_j^2 \frac{m_k^*}{\alpha_k}\phi_{k,j}(1) - X_i\phi_{k,j}'''(0) + \int_0^1 \phi_{k,i}''\phi_{k,j}''ds \tag{19}$$

Substituting (19) into (20) yields

$$\sum_{k=1}^{N_b} \Bigg[-\mu_k \omega_j^2 \int_0^1 \phi_{k,i}\phi_{k,j}ds - \omega_j^2 m_k^* \phi_{k,i}(1)\phi_{k,j}(1) - \alpha_k X_i \phi_{k,j}'''(0) + \alpha_k \int_0^1 \phi_{k,i}''\phi_{k,j}''ds \Bigg] \tag{20}$$

$$-\mu \omega_j^2 X_i X_j + K^* X_i X_j + X_i \sum_{k=1}^{N_b} \alpha_k \phi_{k,j}'''(0) = 0$$

which gets simplified into

$$-\omega_j^2 \left[\sum_{k=1}^{N_b} \mu_k \int_0^1 \phi_{k,i}\phi_{k,j}ds + \mu X_i X_j + \sum_{k=1}^{N_b} m_k^* \phi_{k,i}(1)\phi_{k,j}(1) \right] \tag{21}$$

$$+ \left[\sum_{k=1}^{N_b} \alpha_k \int_0^1 \phi_{k,i}''\phi_{k,j}''ds + K^* X_i X_j \right] = 0 \tag{22}$$

We let

$$M_{ij} = \left[\sum_{k=1}^{N_b} \mu_k \int_0^1 \phi_{k,i}\phi_{k,j}ds + \mu X_i X_j + \sum_{k=1}^{N_b} m_k^* \phi_{k,i}(1)\phi_{k,j}(1) \right] \tag{23}$$

$$K_{ij} = \left[\sum_{k=1}^{N_b} \alpha_k \int_0^1 \phi_{k,i}''\phi_{k,j}''ds + K^* X_i X_j \right] \tag{24}$$

so that Equation (21) becomes

$$-\omega_j^2 M_{ij} + K_{ij} = 0. \tag{25}$$

Note that the normalization condition is set to be $M_{jj} = 1$, which yields

$$\sum_{k=1}^{N_b} \mu_k \int_0^1 \phi_{k,j}\phi_{k,j}ds + \mu X_j X_j + \sum_{k=1}^{N_b} m_k^* \phi_{k,j}(1)\phi_{k,j}(1) = 1. \tag{26}$$

This allows to compute the coefficients $\{a_1, \ldots, a_{N_b}\}$ of the eigenvectors. In particular, the $(N_b - 1)$ coefficients $\{a_2, \ldots, a_{N_b}\}$ are first obtained as function of a_1 through the system $A_{ij}a_j = 0$ (for $i = 2, \ldots, N_b$), and finally a_1 is computed by imposing the previous normalization condition. According to this mass normalization, the frequencies are obtained as

$$\omega_j^2 = K_{jj} = \sum_{k=1}^{N_b} \alpha_k \int_0^1 \phi_{k,j}''\phi_{k,j}''ds + K^* X_j X_j \tag{27}$$

Numerical results. The mode shapes of the system, together with the corresponding natural frequencies, are computed using the linear equations of motion and solving the associated eigenvalue problem discussed in the previous section. Here and henceforth, we will consider $N_b = 4$ microcantilevers attached to the shuttle mass.

The shuttle stiffness is set according to the formula $k = \omega^2 M$, ω being a percentage of the lowest natural frequency of the sensors. The mechanical parameters are set to the following parameters: $k = 10^5$ N/m, $M = 40 \rho Al$, $\rho = 1236$ kg/m^3, $h = b = 50 \, \mu$m, $E_M = 2.8$ GPa, $E_C = 970$ GPa, $\nu_M = 0.3$, $\nu_C = 0.1$, $l = 270 \mu$m. Here, ρ is the mass density of the beam hosting matrix (i.e., epoxy), and h and b are the thickness and width of the microcantilevers cross section, respectively, so that $A = h \, b$ is the area and $J_{22} = 1/12 \, bh^3$ is the second moment of area of the microbeam cross section about the $\mathbf{e}_2$-axis (see Figure 1).

The four microbeams are characterized by increasing volume fractions (from left- to right-beam), respectively $\phi_C = \{2, 3, 5, 7\}\%$. The lowest 13 eigenvalues and the corresponding eigenmodes are depicted in Figure 2; the 1st mode with $\omega_1 = 4.7423$ since it just involves the translational motion of the shuttle mass with no bending of the beams. The higher modes can be classified as local modes encompassing only the flexural motion of each cantilever separately. This indeed makes it possible to use the device as a multimass detector. In particular the 2nd mode, the first flexural of the first microcantilever, is associated with a frequency which is almost twice that of the 1st mode.
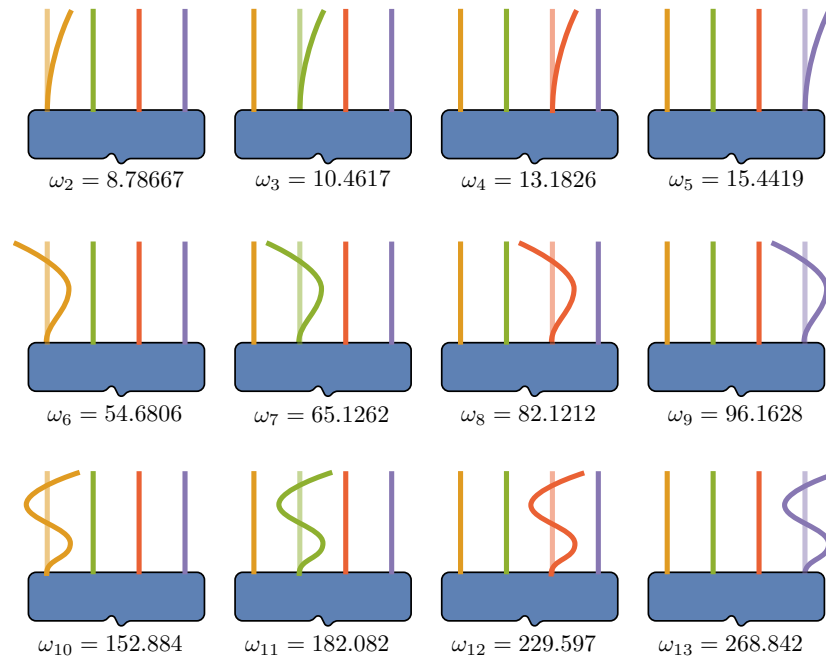
Figure 2. Mode shapes of the device, from the 2nd to the 13rd mode. The 1st mode with $\omega_1 = 4.7423$, involving only the translational motion of the shuttle mass with no bending of the beams, is here omitted.

A parametric analysis is initially performed in order to investigate the sensitivity of the eigenfrequencies with respect to the CNT content variation and beam length. In Figure 3 the first five frequencies are computed by varying the CNT volume fraction separately for each beam. Each curve shows that starting from certain values of the volume fraction, the five eigenfrequencies gain a plateaux, thus indicating a level of CNT content that does not affect the frequency properties of the system. This occurs for the shuttle mass eigenfrequency (*i.e.*, the first one of the SISO system), for small values of CNT volume fraction (about 0.5%), for any beam considered. The same behaviour can be observed for each beam eigenfrequency, although this occurs for values of volume fraction ϕ_C larger and larger. In the same Figure 3 we also indicate through dashed grid lines the values of ϕ_C selected for the next computations, thus proving to have an adequate frequency gap of the system.

The influence of the beam length is also considered in Figure 4: the natural frequency of a beam made by a nanocomposite is compared with the natural frequency of a beam made of silicon in terms of the ratio $\omega_{\text{cnt}}/\omega_{\text{sil}}$ between the 1st natural frequency of the nanocomposite beam and that of the silicon beam, respectively. We explore in Figure 4 how this ratio varies either by increasing the beam nominal length of 270μm by an amplification factor $r \in [0, 4]$, and by increasing the CNT volume fraction, starting from a nominal value of 2% then amplified again by r. While the natural frequency ratio monotically increases as the CNT volume fraction increases, by considering longer and longer lengths of CNT beam made of the same mixture, the natural frequency ratio tends to a plateaux. In particular, a nanocomposite beam with a 2.8% CNT volume fraction has the same value of the 1st natural frequency of a silicon beam of equal length.
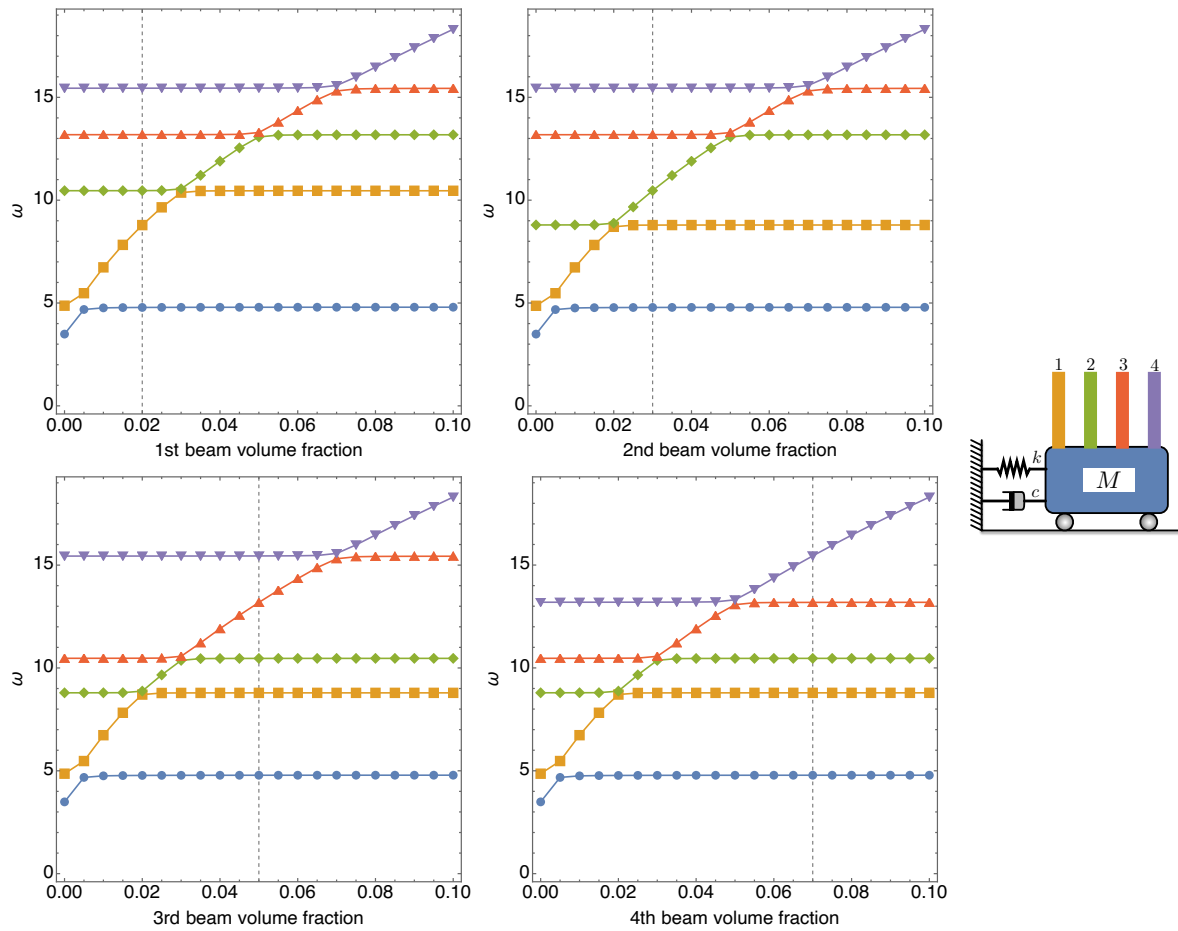
Figure 3. Device frequencies (from the first up to the fifth mode) varying the CNT volume fraction of each beam (beam ordered as the picture on the right). Dashed grid lines indicate the opted values in the analyses for the chosen volume fractions for the subsequent analyses.
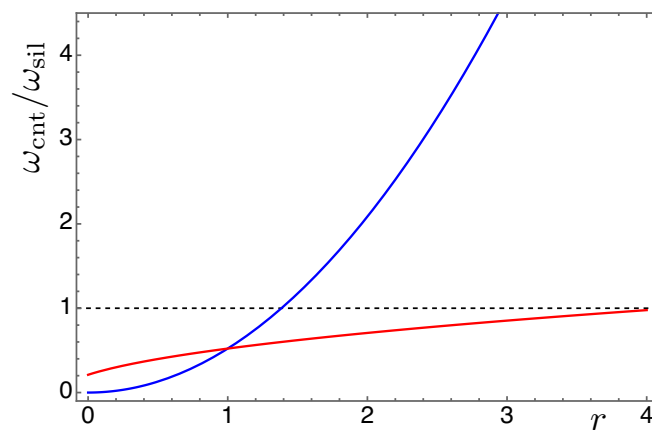

Figure 4. Natural frequencies ratio of a beam made by a nanocomposite (ω_{cnt}) with respect to a beam made of silicon (ω_{sil}). Ratio varying for increasing beam length as $r\,270\mu$m of the silicon beam (blue curve), and ratio varying for increasing volume fraction as $r\,0.02$ of the CNT beam (red curve).

If one chooses to set the first frequency of a microbeam to a certain target frequency, the microbeam could be designed in terms of a suitable length and CNT volume fraction. Figure 5 shows indeed how to reduce the beam length as the CNT volume fractions increases. In particular, to have the same first frequency a silicon-made microbeam would be twice as long as a microbeam of nanocomposite

with very low CNT volume fraction; a 8%-CNT nanocomposite beam has the same first frequency of a silicon microbeam of equal length.
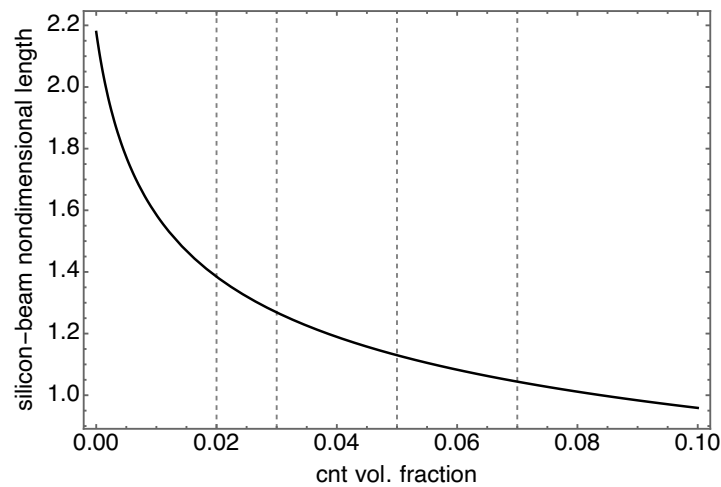

Figure 5. Dependency of silicon-beam length on nanocomposite-beam volume fraction to have the same first beam natural frequency. The silicon-beam length is adimenzionalized with respect to the nanocomposite-beam length equal to 270μm. Gridlines denote the volume fraction values used in the device.

4. Frequency Response Analysis

The Galerkin method is adopted to reduce the nonlinear integral-partial-differential equations of motion into a reduced-order model (ROM). By setting the unknown vector

$$\mathbf{v}(s,t)^\top = [x(t), v_1(s,t), v_2(s,t), ..., v_{N_b}(s,t)] \tag{28}$$

the full system of equation can be cast as

$$\mathbf{I}\ddot{\mathbf{v}} + \mathbf{L}\mathbf{v} = -\mathbf{n}(\mathbf{v}, \dot{\mathbf{v}}, \ddot{\mathbf{v}}) + \mathbf{f} \tag{29}$$

where $\mathbf{I}$ and $\mathbf{L}$ are the generalized inertia and stiffness operators, $\mathbf{n}$ is the vector collecting the nonlinear terms, and $\mathbf{f}$ is the vector of external forces. By expressing the solution as

$$\mathbf{v}(s,t)^\top = [q_1(t)\,X_1,\ \sum_{j=2}^{N_m} q_j(t)\mathbf{u}_j(s)]^\top \tag{30}$$

where we considered the jth mode $\mathbf{u}_j^\top = [X_1, \phi_{k,j}(s)]$, for $k = 1, \dots N_b$, and substituting it into (29) yields

$$\ddot{q}_j\mathbf{I}\mathbf{u}_j + q_j\mathbf{L}\mathbf{u}_j = -\mathbf{n}(q_j\mathbf{u}_j, \dot{q}_j\mathbf{u}_j, \ddot{q}_j\mathbf{u}_j) + \mathbf{f} \tag{31}$$

where the summation convention has been adopted. Multiplying by $\mathbf{u}_i^\top$ and integrating over $[0,1]$ yields the Galerkin discretized equations

$$\ddot{q}_j \int_0^1 \mathbf{u}_i^\top \mathbf{I}\mathbf{u}_j ds + q_j \int_0^1 \mathbf{u}_i^\top \mathbf{L}\mathbf{u}_j ds = -\int_0^1 \mathbf{u}_i^\top \mathbf{n}(q_j\mathbf{u}_j, \dot{q}_j\mathbf{u}_j, \ddot{q}_j\mathbf{u}_j)ds + \int_0^1 \mathbf{u}_i^\top \mathbf{f} ds \tag{32}$$

which can be rewritten as

$$M_{ij}\ddot{q}_j + K_{ij}q_j + n_i = f_i \cos \Omega t \tag{33}$$

where

$$n_i = \int_0^1 \mathbf{u}_i^\top \mathbf{n}(q_j\mathbf{u}_j)ds, \quad f_i = \int_0^1 \mathbf{u}_i^\top \mathbf{f}ds \qquad (34)$$

By taking one trial function for each cantilever, a 5-dof overall ROM is obtained (i.e., 1 dof for the shuttle mass and 1 dof for each of the four microcantilevers). This approach was shown to be acceptable in [43,45] where a convergence analysis was carried out. We will also consider the parameters $\zeta_M = 0.01$ and $\zeta = 0.011$ for the shuttle mass damping ratio and the microcantilevers damping ratio, respectively; all the other mechanical parameters are those reported in the previous section.

In order to obtain the periodic responses and the frequency response curves, we employed the adaptive pseudo-arclength pathfollowing procedure proposed in [45], developed by some of the authors and freely available on the Zenodo repository website: https://doi.org/10.5281/zenodo.6616482. In particular, the search of periodic solutions is based on computing the fixed points of the Poincaré map whose Jacobian turns out to be the monodromy matrix, whose eigenvalues are the Floquet multipliers which dictate the stability of the periodic solutions [46,47]. The Jacobian matrix of the Poincaré map is calculated according to a finite difference approach in state space, and it works as iteration matrix. The interested reader can find further details in [45].

The dynamic behavior of the device is investigated by computing the frequency response curves for different device configurations, in particular, accounting for the case of additional masses m_j at the tip of the jth microcantilever; unless otherwise stated, we set for $m_j^* = 0.01$, *i.e.*, 1% of the microcantilever mass (ρAl is about 835 pg).Finally, we took as characteristic frequency, the first bending frequency of a microbeam made of neat polymer, so that $\omega_c = 345,755$ rad/s.

In the following, we present and discuss some numerical results aimed at demonstrating the sensitivity of the SISO system to the presence of additional tip masses. Note that in all figures reporting the frequency response curves of the SISO system, thin curves are referred to systems without tip masses, thick curves to systems with tip masses.

The frequency response curves reported in Figures 6–8 are recovered in a frequency bandwidth close to the frequencies of the lowest bending modes of the microbeams. We tested four SISO configurations: a system without additional masses, a system where a tip mass is added to the first (from left) microbeam, another system with tip masses at both the first and the third microbeam, and finally a system with tip masses deposited on all microbeams. Such figures show that the frequency shift is bounded within a narrow frequency bandwidth close to the frequency peak of the microbeams with mass absorbed at the tip. The comparison also proves that the sensitivity increases with the frequency of the considered local vibration mode, and it is in line with similar results reported in the literature obtained for simple microstructures (e.g., microcantilevers or clamped-clamped microbeams), see [48,49].

Similar qualitative results can be found in Figures 9–11 which report frequency response curves for the same four SISO configurations when the excitation frequency is increased until nearing to the frequency of the second bending mode of the microbeams. The nonlinearities of the system entail a higher sensitivity than that predicted by the linear model, thus proving that nonlinear effects are advantageous to ensure higher performance of the MEMS mass sensor system. In fact, 1% deposited mass produces a shift of the peak about 0.125 in nondimensional frequency around the first mode, while such a value is amplified about by ten times around the second mode.
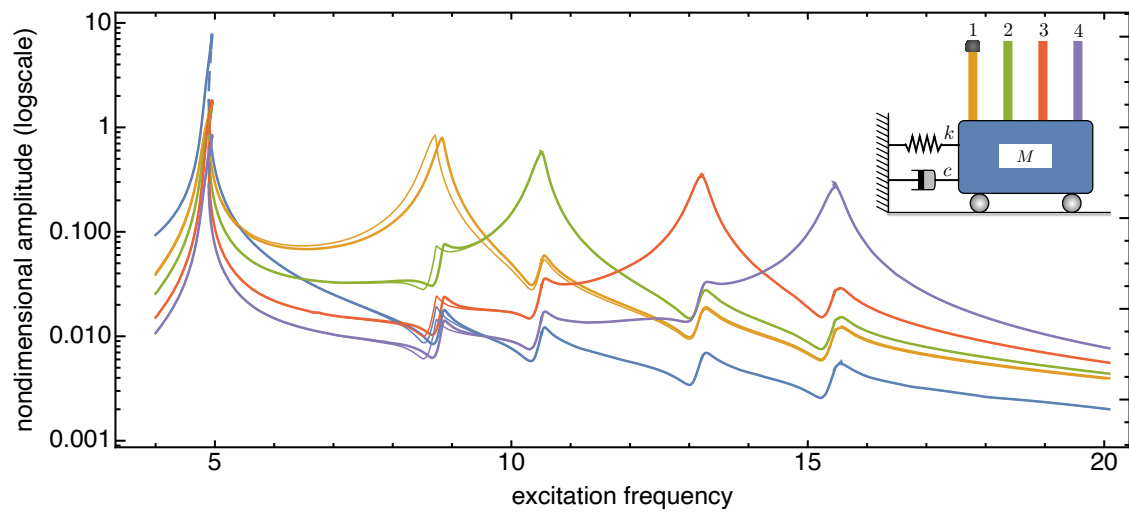
Figure 6. Frequency response curves of the device with and without tip mass when the 1% added mass is absorbed onto the first microcantilever tip (from left).
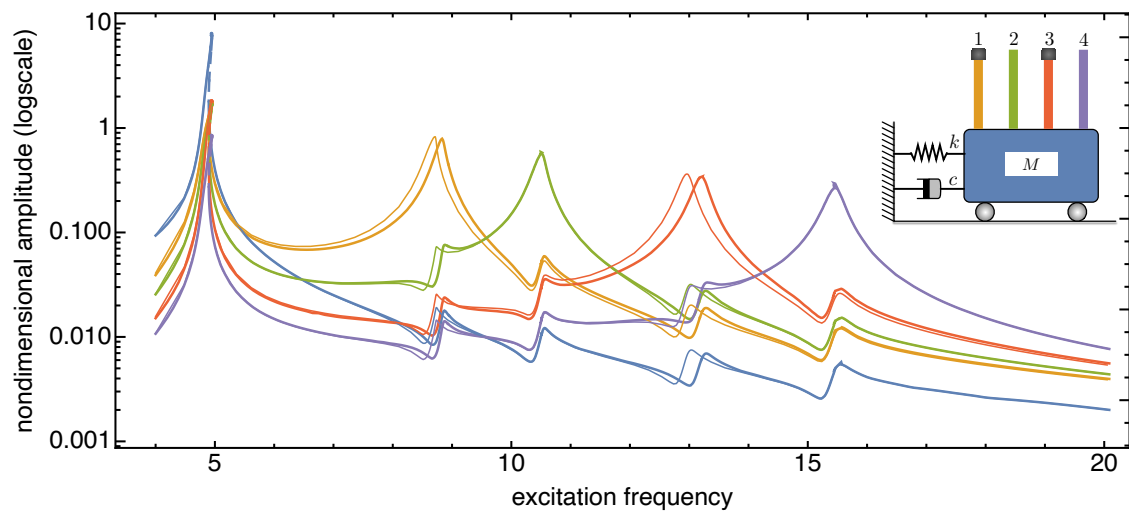
Figure 7. Frequency response curves of the device with and without tip mass when the added mass is absorbed onto both the tips of the first and third microcantilevers.
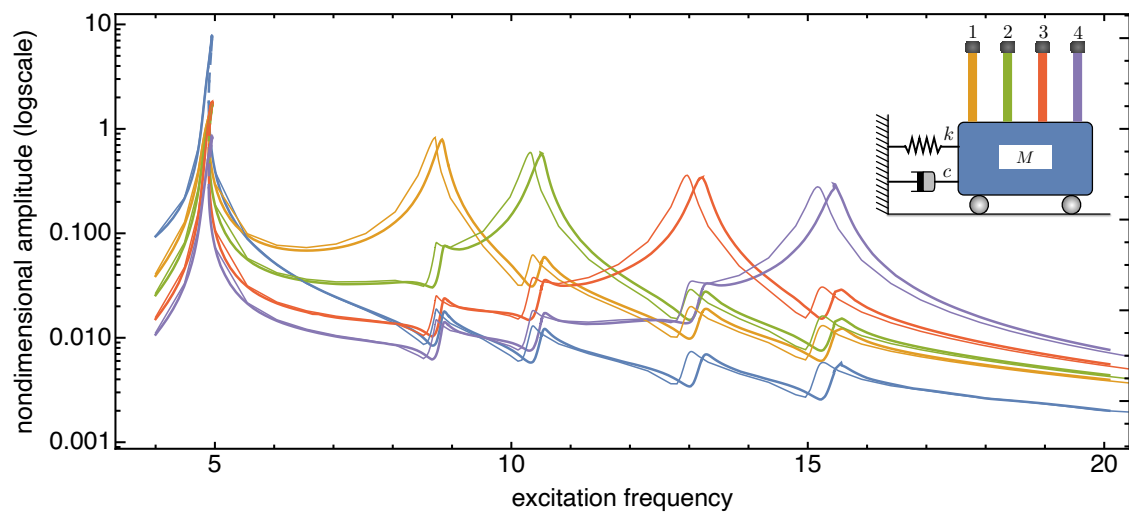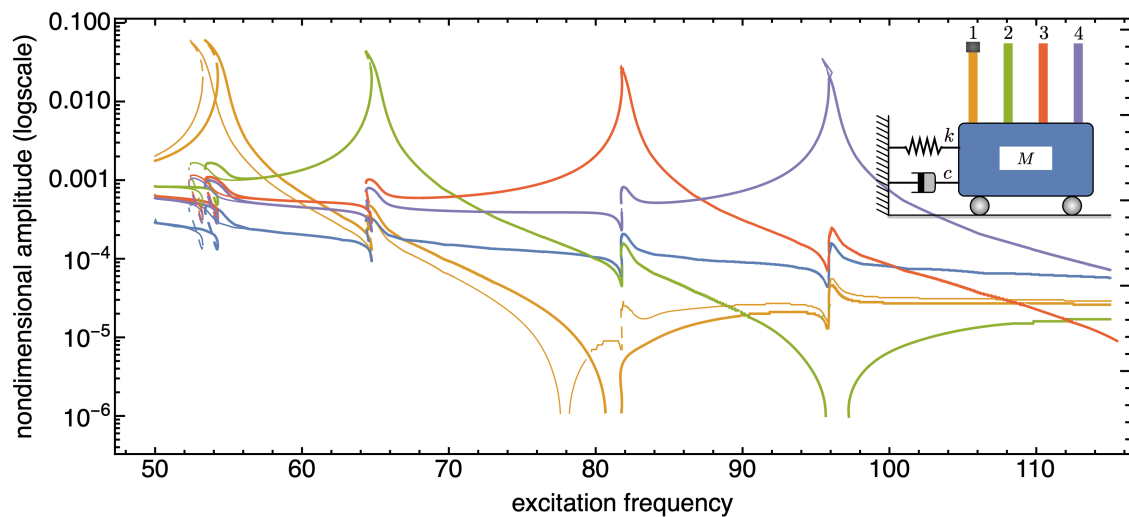
Figure 8. Frequency response curves of the device with and without tip mass when the added mass is absorbed onto all the microcantilevers tips.

Figure 9. Frequency response curves of the device with and without tip mass when the 1% tip mass is absorbed onto the first microcantilever tip (from left). Frequency bandwidth restricted to the second bending modes of the microcantilevers.
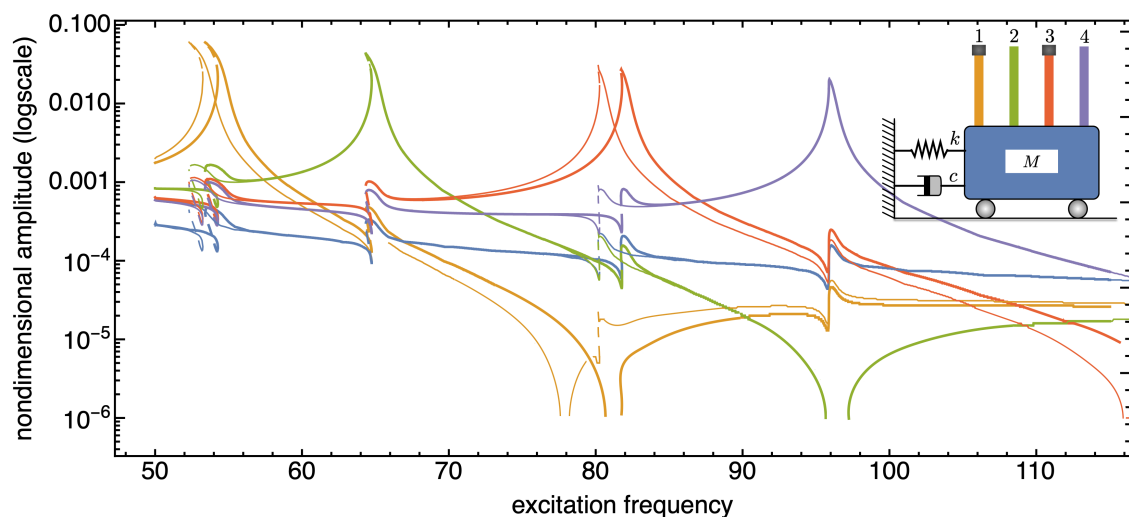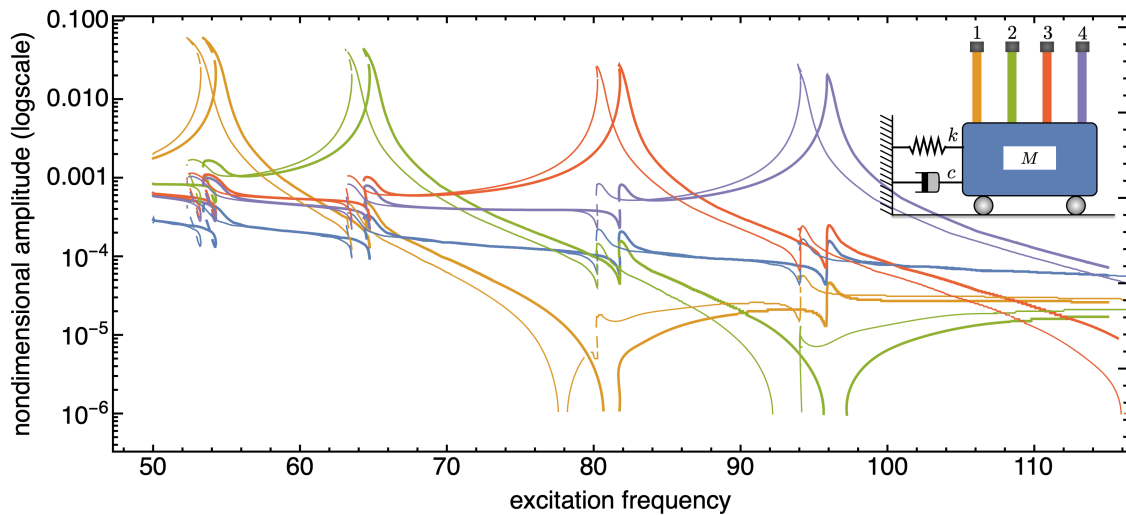

Figure 10. Frequency response curves of the device with and without tip mass when the tip mass is absorbed onto both the tips of the first and third microcantilevers. Frequency bandwidth restricted to the second bending modes of the microcantilevers.

Figure 11. Frequency response curves of the device with and without tip mass when the tip mass is absorbed onto all the microcantilevers tips. Frequency bandwidth restricted to the second bending modes of the microcantilevers.

Such a mass sensitivity is further investigated for increasing values of additional masses. We assume to add the tip mass just to the first (from left) microbeam. Figures 12 and 13 show the frequency response curves limited to tip deflection of such a beam, with excitation frequency ranging in values around the first and the second mode, respectively.

Such figures not only reveal the expected trend of the resonance peak shift upon increasing the tip mass, but they also highlight a change in the length of the unstable branch of the response curve. In fact, around the first mode frequency, the shift in frequency occurs with a hardening nonlinear response which becomes more and more evident (see Figure 12); on the other hand, around the second mode frequency, the softening nonlinear response does not change much qualitatively (see Figure 13).
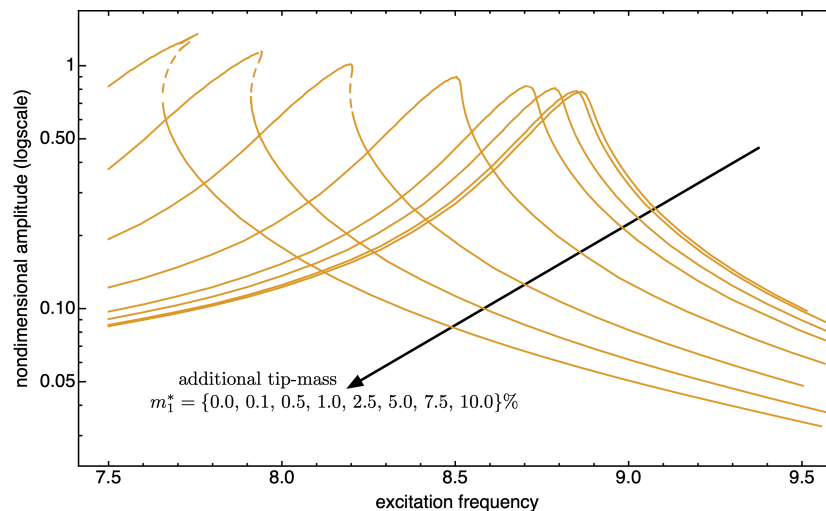

Figure 12. Absorbed mass sensitivity. Frequency response curves of the first bending mode of the first cantilever with an additional mass at the tip. See also Figure 6.
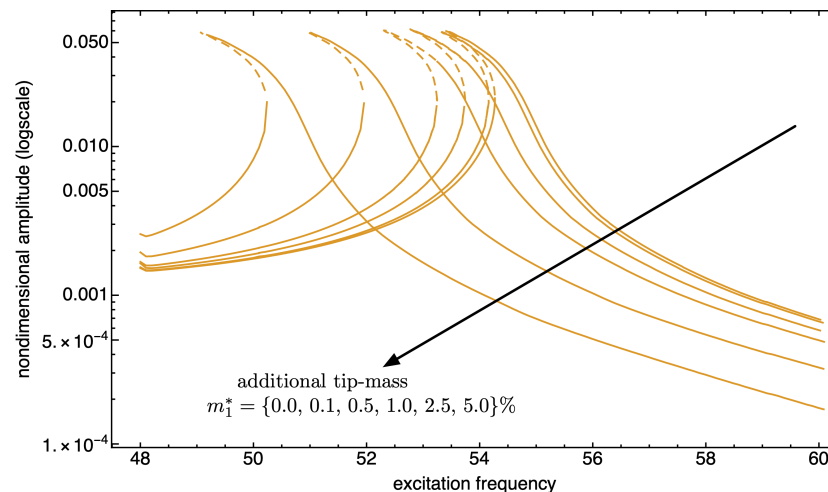
Figure 13. Absorbed mass sensitivity. Frequency response curves of the second bending mode of the first cantilever with an additional mass at the tip. See also Figure 9.

5. Conclusions

In this work the operating principles of a nonlinear MEMS multi-mass sensor are investigated. The device consists of an array of microcantilevers, made of carbon nanotube nanocomposite material, possessing a functionalized surface at their tips that can absorb molecules of target materials. The microcantilever sensors are clamped onto a shuttle mass which, in turn, is subject to electrostatic excitation. The system is treated as a single input-single output (SISO) system. Each microcantilever is modeled as a nonlinear Euler-Bernoulli beam undergoing a moderately large resonance motions. The modal characteristics of the mechanical system are investigated carrying out a parametric study varying the CNT volume fraction in each microbeam. The frequency response and stability are investigated by path following the periodic solutions of the device near the lowest three bending modes of the microcantilevers. The main finding is that the dynamic mass sensitivity measured as frequency shifts induced by the target mass absorbed at the cantilevers tip is enhanced by the nonlinear resonances of the microcantilevers modes, especially for higher modes. Moreover, it is shown that the fine tuning of the frequencies of the microcantilevers effected by the carbon nanotube content in the nanocomposite material paves the way towards an effective design of multimass sensors since the microcantilevers may self-detect their motion exploiting the electrical conductivity of the CNT nanocomposites.

Appendix A. Eigenproblem

The linearized equations of motion are

$$\rho A(\partial_{tt}w_j + \partial_{tt}x) + EJ_j^{\text{eq}}\partial_{ssss}w_j = 0$$

$$M\partial_{tt}x + Kx + \sum_j EJ_j^{\text{eq}}\partial_{sss}w_j\big|_{s=0} = 0,$$

(A1)

together with the associated boundary conditions for the *j*th microbeam

$$w_j\big|_{s=0} = 0 = \partial_s w_j\big|_{s=0}$$

(A2)

$$EJ_j^{\text{eq}}\partial_{ss}w_j\big|_{s=l} = 0, \quad EJ_j^{\text{eq}}\partial_{sss}w_j\big|_{s=l} = m_j\left(\partial_{tt}x + \partial_{tt}w_j\big|_{s=l}\right)$$

(A3)

Let $w_j(s,t) = \exp(i\omega t)\phi_j(s) + cc$ and $x(t) = \exp(i\omega t)X + cc$ where i is the imaginary unit and ω the circular frequency. Substituting the above equation into (A7) and (A12) yields

$$-\rho A\omega^2(\phi + X) + EJ_j^{\text{eq}}\partial_{ssss}\phi_j = 0$$

$$-M\omega^2 X + KX + \sum_k EJ_k^{\text{eq}}\partial_{sss}\phi_k(0) = 0$$

(A4)

The associated boundary conditions for the beams are

$$\phi_j(0) = 0 = \partial_s\phi_j(0)$$

(A5)

$$EJ_j^{\text{eq}}\partial_{ss}\phi_j(l) = 0, \quad EJ_j^{\text{eq}}\partial_{sss}\phi_j(l) = -m_j\omega^2(X + \phi(l))$$

(A6)

Setting total displacement $v_j(s,t) = x(t) + w_j(s,t)$

$$\rho A\partial_{tt}v_j + EJ_j^{\text{eq}}\partial_{ssss}v_j = 0$$

$$M\partial_{tt}x + Kx + \sum_k EJ_k^{\text{eq}}\partial_{sss}v_k\big|_{s=0} = 0$$

(A7)

The associated boundary conditions for the beams are

$$w\big|_{s=0} - x(t) = 0, \quad \partial_s v_j\big|_{s=0} = 0$$

(A8)

$$EJ_j^{\text{eq}}\partial_{ss}v_j\big|_{s=l} = 0, \quad EJ_j^{\text{eq}}\partial_{sss}v_j\big|_{s=l} = m_j\partial_{tt}v_j\big|_{s=l}$$

(A9)

Let $v_j(s,t) = \exp(i\omega t)\phi_j(s) + cc$ and $x(t) = \exp(i\omega t)X + cc$ where i is the imaginary unit and ω the circular frequency. Substituting the above equation into (A7) and (A12) yields

$$-\rho A_j\omega^2\phi_j + EJ_j^{\text{eq}}\partial_{ssss}\phi_j = 0$$

(A10)

$$-M\omega^2 X + KX + \sum_k EJ_k^{\text{eq}}\partial_{sss}\phi_k(0) = 0$$

(A11)

The associated boundary conditions for the beams are

$$\phi_j(0) - X = 0 \quad \partial_s\phi_j(0) = 0$$

(A12)

$$EJ_j^{\text{eq}}\partial_{ss}\phi_j(l) = 0, \quad EJ_j^{\text{eq}}\partial_{sss}\phi_j(l) + m_j\omega^2\phi(l) = 0$$

(A13)

Let $\phi_j(s) = B_j\exp(\lambda_j s)$ and substitute into (A15) to obtain

$$-\rho A_j\omega^2 B_j + EJ_j^{\text{eq}}B_j\lambda_j^4 = 0$$

(A14)

From the first equation

$$\lambda_j^2 = \pm\omega\beta_j \tag{A15}$$

where $\beta_j^2 = (\rho A_j)/(EJ_j^{\text{eq}})$, $\Lambda_j = \sqrt{\omega\beta_j}$ from which $\lambda_j = (\pm\Lambda_j, \pm i\Lambda_j)$

The microbeam mode shape can be expressed as

$$\phi_j = a_j \cos\Lambda_j s + b_j \sin\Lambda_j s + c_j \sinh\Lambda_j s + d_j \cosh\Lambda_j s \tag{A16}$$

On the other hand, the modal component of the shuttle mass is obtained substituting (A16) into (A11) that yields

$$X = \frac{1}{K - M\omega^2} \sum_k EJ_k^{\text{eq}}(b_k - d_k)\Lambda_k^3 \tag{A17}$$

The imposition of the boundary conditions leads to

$$a_j + c_j - \frac{1}{K - M\omega^2} \sum_k EJ_k^{\text{eq}}(b_k - d_k)\Lambda_k^3 = 0, \tag{A18}$$

$$b_j + d_j = 0, \tag{A19}$$

$$-a_j \cos\left(l\Lambda_j\right) - b_j \sin\left(l\Lambda_j\right) + c_j \cosh\left(l\Lambda_j\right) + d_j \sinh\left(l\Lambda_j\right) = 0, \tag{A20}$$

$$\Lambda_j^3 EJ_j^{\text{eq}}\left(a_j \sin\left(l\Lambda_j\right) - b_j \cos\left(l\Lambda_j\right) + c_j \sinh\left(l\Lambda_j\right) + d_j \cosh\left(l\Lambda_j\right)\right) \tag{A21}$$

$$+m_j\omega^2\left(a_j \cos\left(l\Lambda_j\right) + b_j \sin\left(l\Lambda_j\right) + c_j \cosh\left(l\Lambda_j\right) + d_j \sinh\left(l\Lambda_j\right)\right) = 0$$

Equations (A19)–(A21) are solved for (b_j, c_j, d_j) in terms of a_j which, in turn, is substituted into (A18). The determinant of the ensuing coefficient matrix set to zero yields the characteristic equation. For each root of the characteristic equation, i.e., frequency ω_k, the corresponding eigenvector is made of $1 + 4N_b$ components, *i.e.*,

$$(X_k, a_{1,k}, b_{1,k}, c_{1,k}, d_{1,k}, \ldots, a_{k,N_b}, b_{k,N_b}, c_{k,N_b}, d_{k,N_b})$$

where N_b is the number of microbeams. Each sub-eigenvector $(a_{j,k}, b_{j,k}, c_{j,k}, d_{j,k})$ provides the kth modal contribution for the jth beam described by $\phi_{j,k}(s)$.

Finally, notice that Equations (A19)–(A21) can be solved in a_i, ie.:

$$b_i = \bar{b}_i\,a_i, \quad c_i = \bar{c}_i\,a_i, \quad d_i = \bar{d}_i\,a_i,$$

so that Equation (A18) reads as a system of N_b equations

$$(1 + \bar{c}_i)\,a_i + \sum_k \bar{g}_k a_k = 0$$

to be solved for nontrivial solutions, *i.e.*, $\det(\mathbf{A}) = 0$, associated with the matrix $\mathbf{A}$ whose components are $A_{ij} = (1 + \bar{c}_j)\,\delta_{ij} + \bar{g}_j$.

References

1. Younis, M.I. *MEMS Linear and Nonlinear Statics and Dynamics*; Vol. 20, Springer Science & Business Media, 2011.
2. Kim, P.; Bae, S.; Seok, J. Resonant behaviors of a nonlinear cantilever beam with tip mass subject to an axial force and electrostatic excitation. *Int. J. Mech. Sci.* **2012**, *64*, 232–257.
3. Karličić, D.; Kozić, P.; Adhikari, S.; Cajić, M.; Lazarević, M. Nonlocal mass-nanosensor model based on the damped vibration of single-layer graphene sheet influenced by in-plane magnetic field. *Int. J. Mech. Sci.* **2015**, *96-97*, 132–142.

4.   Fernández-Sáez, J.; Morassi, A.; Rubio, L.; Zaera, R. Transverse free vibration of resonant nanoplate mass sensors: Identification of an attached point mass. *Int. J. Mech. Sci.* **2019**, *150*, 217–225.

5.   Dilena, M.; Dell'Oste, M.F.; Fernández-Sáez, J.; Zaera, R. Mass detection in nanobeams from bending resonant frequency shifts. *Mech. Syst. Signal Process.* **2019**, *116*, 261–276.

6.   Pratiher, B. Stability and bifurcation analysis of an electrostatically controlled highly deformable microcantilever-based resonator. *Nonlinear Dyn.* **2014**, *78*, 1781–1800.

7.   Mahmoodi, S.N.; Jalili, N.; Ahmadian, M. Subharmonics analysis of nonlinear flexural vibrations of piezoelectrically actuated microcantilevers. *Nonlinear Dyn.* **2010**, *59*, 397–409.

8.   Han, J.; Qi, H.; Jin, G.; Li, B.; Feng, J.; Zhang, Q. Mechanical behaviors of electrostatic microresonators with initial offset imperfection: qualitative analysis via time-varying capacitors. *Nonlinear Dyn.* **2018**, *91*, 269–295.

9.   Zaitsev, S.; Shtempluck, O.; Buks, E.; Gottlieb, O. Nonlinear damping in a micromechanical oscillator. *Nonlinear Dyn.* **2012**, *67*, 859–883.

10. Seleim, A.; Towfighian, S.; Delande, E.; Abdel-Rahman, E.; Heppler, G. Dynamics of a close-loop controlled MEMS resonator. *Nonlinear Dyn.* **2012**, *69*, 615–633.

11. Towfighian, S.; Heppler, G.R.; Abdel-Rahaman, E.M. Low-voltage closed loop MEMS actuators. *Nonlinear Dyn.* **2012**, *69*, 565–575.

12. Wang, J.; Yang, J.; Chen, D.; Jin, L.; Li, Y.; Zhang, Y.; Xu, L.; Guo, Y.; Lin, F.; Wu, F. Gas Detection Microsystem with MEMS Gas Sensor and Integrated Circuit. *IEEE Sensors J.* **2018**.

13. Urasinska-Wojcik, B.; Vincent, T.A.; Chowdhury, M.F.; Gardner, J.W. Ultrasensitive WO3 gas sensors for NO2 detection in air and low oxygen environment. *Sensors Actuators B Chem.* **2017**, *239*, 1051–1059.

14. Liu, Y.; Xu, X.; Chen, Y.; Zhang, Y.; Gao, X.; Xu, P.; Li, X.; Fang, J.; Wen, W. An integrated micro-chip with Ru/Al2O3/ZnO as sensing material for SO2 detection. *Sensors Actuators B Chem.* **2018**, *262*, 26–34.

15. Gerdroodbary, M.B.; Anazadehsayed, A.; Hassanvand, A.; Moradi, R. Calibration of low-pressure MEMS gas sensor for detection of hydrogen gas. *Int. J. Hydrog. Energy* **2018**, *43*, 5770–5782.

16. Mahyari, A.; Gerdroodbary, M.B.; Mosavat, M.; Ganji, D. Detection of ammonia gas by Knudsen thermal force in micro gas actuator. *Case Stud. Therm. Eng.* **2018**, *12*, 276–284.

17. Boisen, A.; Dohn, S.; Keller, S.S.; Schmid, S.; Tenje, M. Cantilever-like micromechanical sensors. *Reports on Progress in Physics* **2011**, *74*, 036101.

18. Yu, F.; Yu, H.; Xu, P.; Li, X. Precise extension-mode resonant sensor with uniform and repeatable sensitivity for detection of ppm-level ammonia. *J. Micromechanics Microengineering* **2014**, *24*, 045005.

19. Dorsey, K.; Bedair, S.; Fedder, G. Gas chemical sensitivity of a CMOS MEMS cantilever functionalized via evaporation driven assembly. *J. Micromechanics Microengineering* **2014**, *24*, 075001.

20. Faegh, S.; Jalili, N.; Sridhar, S. Ultrasensitive Piezoelectric-Based Microcantilever Biosensor: Theory and Experiment. *Mechatronics Ieee/Asme Trans.* **2015**, *20*, 308–312.

21. Spletzer, M.; Raman, A.; Wu, A.Q.; Xu, X.; Reifenberger, R. Ultrasensitive mass sensing using mode localization in coupled microcantilevers. *Appl. Phys. Lett.* **2006**, *88*, 254102.

22. Zhao, C.; Montaseri, M.H.; Wood, G.S.; Pu, S.H.; Seshia, A.A.; Kraft, M. A review on coupled MEMS resonators for sensing applications utilizing mode localization. *Sensors Actuators A Phys.* **2016**, *249*, 93–111.

23. Walter, V.; Bourbon, G.; Le Moal, P.; Kacem, N.; Lardiès, J. Electrostatic actuation to counterbalance the manufacturing defects in a MEMS mass detection sensor using mode localization. *Procedia Eng.* **2016**, *168*, 1488–1491.

24. Yabuno, H.; Seo, Y.; Kuroda, M. Self-excited coupled cantilevers for mass sensing in viscous measurement environments. *Appl. Phys. Lett.* **2013**, *103*, 063104.

25. Endo, D.; Yabuno, H.; Higashino, K.; Yamamoto, Y.; Matsumoto, S. Self-excited coupled-microcantilevers for mass sensing. *Applied Physics Letters* **2015**, *106*, 223105.

26. Pallay, M.; Daeichin, M.; Towfighian, S. Dynamic behavior of an electrostatic MEMS resonator with repulsive actuation. *Nonlinear Dyn.* **2017**, *89*, 1525–1538.

27. Singh, T.; Elhady, A.; Jia, H.; Mojdeh, A.; Kaplan, C.; Sharma, V.; Basha, M.; Abdel-Rahman, E. Modeling of low-damping laterally actuated electrostatic MEMS. *Mechatronics* **2018**, *52*, 1–6.

28. Kang, D.K.; Yang, H.I.; Kim, C.W. Geometrically nonlinear dynamic behavior on detection sensitivity of carbon nanotube-based mass sensor using finite element method. *Finite Elem. Anal. Des.* **2017**, *126*, 39–49.

29. Mehdipour, I.; Erfani-Moghadam, A.; Mehdipour, C. Application of an electrostatically actuated cantilevered carbon nanotube with an attached mass as a bio-mass sensor. *Curr. Appl. Phys.* **2013**, *13*, 1463–1469.

30. Azizi, S.; Kivi, A.R.; Marzbanrad, J. Mass detection based on pure parametric excitation of a micro beam actuated by piezoelectric layers. *Microsyst. Technol.* **2017**, *23*, 991–998.

31. Kumar, V.; Boley, J.W.; Ekowaluyo, H.; Miller, J.K.; Marvin, G.C.; Chiu, G.T.C.; Rhoads, J.F. Linear and nonlinear mass sensing using piezoelectrically-actuated microcantilevers. In *MEMS and Nanotechnology, Volume 2*; Springer, 2011; pp. 57–65.

32. Bouchaala, A.; Jaber, N.; Yassine, O.; Shekhah, O.; Chernikova, V.; Eddaoudi, M.; Younis, M.I. Nonlinear-based MEMS Sensors and active switches for gas detection. *Sensors* **2016**, *16*, 758.

33. Bouchaala, A.; Nayfeh, A.H.; Jaber, N.; Younis, M.I. Mass and position determination in MEMS mass sensors: a theoretical and an experimental investigation. *J. Micromechanics Microengineering* **2016**, *26*, 105009.

34. Nguyen, V.N.; Baguet, S.; Lamarque, C.H.; Dufour, R. Bifurcation-based micro-/nanoelectromechanical mass detection. *Nonlinear Dyn.* **2015**, *79*, 647–662.

35. Nayfeh, A.; Ouakad, H.; Najar, F.; Choura, S.; Abdel-Rahman, E. Nonlinear dynamics of a resonant gas sensor. *Nonlinear Dyn.* **2010**, *59*, 607–618.

36. DeMartini, B.E.; Rhoads, J.F.; Zielke, M.A.; Owen, K.G.; Shaw, S.W.; Turner, K.L. A single input-single output coupled microresonator array for the detection and identification of multiple analytes. *Appl. Phys. Lett.* **2008**, *93*, 054102.

37. Pierre, C.; Dowell, E. Localization of vibrations by structural irregularity. *J. Sound Vib.* **1987**, *114*, 549–564.

38. Talò, M.; Krause, B.; Pionteck, J.; Lanzara, G.; Lacarbonara, W. An updated micromechanical model based on morphological characterization of carbon nanotube nanocomposites. *Composites Part B: Engineering* **2017**, *115*, 70–78.

39. Formica, G.; Lacarbonara, W. Three-dimensional modeling of interfacial stick-slip in carbon nanotube nanocomposites. *International Journal of Plasticity* **2017**, *88*, 204–217.

40. Lacarbonara, W.; Guruva, S.K.; Carboni, B.; Krause, B.; Janke, A.; Formica, G.; Lanzara, G. Unusual nonlinear switching in branched carbon nanotube nanocomposites. *Scientific Reports* **2023**, *13*. doi:10.1038/s41598-023-32331-y.

41. Lacarbonara, W. *Nonlinear structural mechanics: theory, dynamical phenomena and modeling*; Springer Science & Business Media, 2013.

42. Formica, G.; Talò, M.; Lacarbonara, W. Nonlinear modeling of carbon nanotube composites dissipation due to interfacial stick–slip. *International Journal of Plasticity* **2014**, *53*, 148–163.

43. Cetraro, M.; Lacarbonara, W.; Formica, G. Nonlinear Dynamic Response of Carbon Nanotube Nanocomposite Microbeams. *Journal of Computational and Nonlinear Dynamics* **2017**, *12*, 031007.

44. Formica, G.; Lacarbonara, W. Asymptotic dynamic modeling and response of hysteretic nanostructured beams. *Nonlinear Dynamics* **2019**, *99*, 227–248. doi:10.1007/s11071-019-05386-8.

45. Formica, G.; Milicchio, F.; Lacarbonara, W. A Krylov accelerated Newton–Raphson scheme for efficient pseudo-arclength pathfollowing. *International Journal of Non-Linear Mechanics* **2022**, *145*, 104116.

46. Lacarbonara, W.; Vestroni, F.; Capecchi, D. Poincaré map-based continuation of periodic orbits in dynamic discontinuous and hysteretic systems. Proceedings of the ASME Design Engineering Technical Conference, 1999, Vol. 7B-1999, pp. 2215–2224. doi:10.1115/DETC99-VIB-8088.

47. Formica, G.; Vaiana, N.; Rosati, L.; Lacarbonara, W. Pathfollowing of high-dimensional hysteretic systems under periodic forcing. *Nonlinear Dynamics* **2021**, *103*, 3515–3528. doi:10.1007/s11071-021-06374-7.

48. Ghatkesar, M.K.; Barwich, V.; Braun, T.; Ramseyer, J.P.; Gerber, C.; Hegner, M.; Lang, H.P.; Drechsler, U.; Despont, M. Higher modes of vibration increase mass sensitivity in nanomechanical microcantilevers. *Nanotechnology* **2007**, *18*, 445502.

49. Bouchaala, A.; Nayfeh, A.H.; Younis, M.I. Analytical study of the frequency shifts of micro and nano clamped–clamped beam resonators due to an added mass. *Meccanica* **2017**, *52*, 333–348.